

HOLESOM: Constraining the Properties of Slowly-Accreting Massive Black Holes with Self-Organizing Maps

VALENTINA LA TORRE^{1,2} AND FABIO PACUCCI^{1,3}

¹*Center for Astrophysics | Harvard & Smithsonian, 60 Garden St, Cambridge, MA 02138, USA*

²*Department of Physics and Astronomy, Tufts University, Medford, MA 02144, USA*

³*Black Hole Initiative, Harvard University, Cambridge, MA 02138, USA*

ABSTRACT

Accreting massive black holes (MBHs, with $M_{\bullet} > 10^3 M_{\odot}$) are known for their panchromatic emission, spanning from radio to gamma rays. While MBHs accreting at significant fractions of their Eddington rate are readily detectable, those accreting at much lower rates in radiatively inefficient modes often go unnoticed, blending in with other astrophysical sources. This challenge is particularly relevant for gas-starved MBHs in external galaxies and those possibly wandering in the Milky Way. We present HOLESOM, a machine learning-powered tool based on the Self-Organizing Maps (SOMs) algorithm, specifically designed to identify slowly-accreting MBHs using sparse photometric data. Trained on a comprehensive set of $\sim 20,000$ spectral energy distributions (SEDs), HOLESOM can (i) determine if the photometry of a source is consistent with slowly-accreting MBHs and (ii) estimate its black hole mass and Eddington ratio, including uncertainties. We validate HOLESOM through extensive tests on synthetic data and real-world cases, including Sagittarius A* (Sgr A*), demonstrating its effectiveness in identifying slowly-accreting MBHs. Additionally, we derive analytical relations between radio and X-ray luminosities to further constrain physical parameters. The primary strength of HOLESOM lies in its ability to accurately identify MBH candidates, which can then be targeted for follow-up photometric and spectroscopic observations. Fast and scalable, HOLESOM offers a robust framework for automatically scanning large multi-wavelength datasets, making it a valuable tool for unveiling hidden MBH populations in the local Universe.

Keywords: Accretion (14) — Intermediate-mass black holes (816) — Supermassive black holes (1663) — Surveys (1671) — Neural networks (1933)

1. INTRODUCTION

Actively accreting black holes are the archetypal panchromatic astrophysical objects. Their surrounding environment is the theater of complex physical processes within, e.g., their accretion disk (Shakura & Sunyaev 1976), corona (Haardt & Maraschi 1991) and jet (Blandford & Znajek 1977), resulting in an electromagnetic spectrum that extends from the radio to gamma rays (Elvis et al. 1994; Shang et al. 2011; Mullaney et al. 2011).

Multi-wavelength studies of Active Galactic Nuclei, or AGN, are powerful tools for studying massive black hole (MBH, $M_{\bullet} > 10^3 M_{\odot}$) growth at high- z (e.g., Volonteri & Rees 2005), testing General Relativity (e.g., Psaltis et al. 2020), and understanding the evolution of galaxies (e.g., Ferrarese & Merritt 2000; Gebhardt et al. 2000). Available data have proliferated over the last 30 years

thanks to dedicated all-sky and pointed surveys at many different wavelengths.

MBHs are detected at the center of most massive galaxies, and tight relations between their mass and their host’s physical properties testify to their co-evolution (Magorrian et al. 1998; Ferrarese & Merritt 2000; Gebhardt et al. 2000; Kormendy & Ho 2013; Reines & Volonteri 2015; Pacucci et al. 2023). While occupying a tiny volume in the cores of their host galaxies, MBHs have an oversized impact on the evolution of the entire galaxy via their feedback (e.g., Di Matteo et al. 2005; Sijacki et al. 2007; Schawinski et al. 2007; Greene et al. 2020). Despite different and, in principle, unrelated growth modes, galaxies and their SMBHs are locked in a cosmic dance of co-evolution. A complete picture of the evolution of galaxies, the building blocks of our Universe, ultimately requires a complete understanding of black holes’ growth and feedback processes.

The population of highly-accreting MBHs contained in AGN is well studied in the local Universe, with surveys (e.g., the Swift-BASS, Ananna et al. 2017, 2022; Koss et al. 2022) able to represent an unbiased picture of the AGN luminosity function, the black hole mass function (BHMF), and the Eddington ratio distribution function (ERDF), where the Eddington ratio is defined as:

$$f_{\text{Edd}} = \frac{\dot{M}_{\bullet}}{\dot{M}_{\text{Edd}}}, \quad (1)$$

where \dot{M}_{Edd} is the mass accretion rate at which a relativistic thin accretion disk (Novikov & Thorne 1973) would radiate at the Eddington luminosity (see, e.g., the discussion in Pacucci & Narayan 2024), and \dot{M} is the mass accretion rate onto the MBH. In general, the radiated luminosity L is related to the accretion rate \dot{M} via $L = \epsilon \dot{M} c^2$, where ϵ is the matter-to-energy radiative efficiency. In the standard, thin-disk accretion scenario (Shakura & Sunyaev 1976), valid for $10^{-2} \lesssim f_{\text{Edd}} \lesssim 1$, the matter-to-energy radiative efficiency is $\epsilon \approx 10\%$ and depends on the black hole spin (Bardeen 1970; Thorne 1974). Highly-accreting MBHs are also observed at high redshifts, with the farthest confirmed AGN now standing at $z = 10.6$ (Maiolino et al. 2023), although the sample completeness is much lower in these cases.

On the contrary, even in the local Universe, the population of MBHs accreting at very low rates ($f_{\text{Edd}} < 10^{-2}$) is sparsely studied. For such low rates, the radiative efficiency ϵ decreases dramatically, possibly by orders of magnitude, as we enter the domain of advection-dominated accretion flows (ADAF, Narayan & Yi 1994; Abramowicz et al. 1995; Narayan & McClintock 2013). As the conditions for large accretion rates are rare, especially at low redshift (Power et al. 2010), most MBHs likely accrete in ADAF mode (Narayan et al. 2022). An example of such objects is the SMBH at the center of the Milky Way (MW): Sagittarius A* (Sgr A*, in short). Recently imaged by the Event Horizon Telescope collaboration (Event Horizon Telescope Collaboration et al. 2022), this SMBH is accreting at $f_{\text{Edd}} \sim 10^{-7}$ (see, e.g., Ressler et al. 2018) and was initially detected by studying the dynamics of the stars in its immediate vicinity (Ghez et al. 2000; Genzel et al. 2000).

Using various methodologies, spanning radio (Reines et al. 2020), optical (Reines et al. 2013), X-ray (Baldassare et al. 2015), and coronal lines (Molina et al. 2021), several samples of tens or even hundreds of MBHs in local dwarf galaxies exist, with typical distances up to ~ 200 Mpc. However, these surveys are biased towards intrinsically brighter MBHs, with an emission significantly brighter than other sources of stellar origin. For example, a $10^5 M_{\odot}$ MBH has to radiate at $\sim 10\%$ of its

Eddington luminosity to produce detectable broad H α that is discernible within 200 Mpc (Reines et al. 2013). A $10^4 M_{\odot}$ MBH would need to accrete at Eddington. These numbers are $10^6 - 10^7$ times higher than the Eddington ratio of Sgr A*. Thus, the population of MBHs with extremely low accretion rates, similar to that of Sgr A*, is, arguably, entirely unexplored.

Detecting electromagnetically MBHs accreting at $f_{\text{Edd}} \ll 1$, even in the very local Universe, is challenging because these sources appear unremarkable in their field and can be easily confused with other sources of stellar origin or even with background, high- z sources. Albeit at a smaller mass scale, a recent attempt to detect electromagnetically the emission from Gaia BH3, a very nearby stellar-mass black hole of $M_{\bullet} \approx 33 M_{\odot}$, led only to an upper limit (Cappelluti et al. 2024).

For these reasons, slowly-accreting MBHs in local galaxies can be selected only via a massively multi-wavelength approach. Such objects can be discerned from other contaminant categories only by collecting numerous photometric points in different bands and comparing this photometry with ADAF SEDs generated either analytically (see, e.g., Mahadevan 1997; Pesce et al. 2021), or with general-relativistic magnetohydrodynamic (GRMHD) simulations of the accretion flow, down to a few gravitational radii (see, e.g., Dolence et al. 2009). The use of advanced computational techniques can lead to a better identification and characterization of such sources.

Machine learning (ML) techniques offer an exciting prospect for selecting and characterizing the physical properties of slowly accreting MBHs in the local Universe. Once a ML technique is trained with the most extensive available set of ADAF SEDs, it learns the patterns between observables and physical underlying parameters, such that it can be deployed to analyze multi-wavelength data fields pertaining to the local Universe. Such codes are easily scalable and can be fed massive amounts of data once proper source-matching techniques between catalogs are used (see, e.g., the software LYRA, Peca et al. 2021).

In this study, we present HOLESOM, a software tool based on the unsupervised ML technique of Self-Organizing Maps. This software represents the first attempt at “black hole cartography”, aimed at identifying and mapping slowly-accreting MBHs in the correct location of the M_{\bullet} vs. f_{Edd} parameter space. This study is organized as follows. In Sec. 2, we present the analytical SEDs used to train our model. Then, Sec. 3 describes the ML methods we employ. In Sec. 4, we present our results. We test our software with artificial (Sec. 4.1) and real-world examples (Sec. 4.2). Then, we show that the

photometry of slowly-accreting MBHs can be effectively disentangled from that of stellar-mass compact objects (Sec.4.3). We also present relationships between radio luminosity, X-ray luminosity, black hole mass and Eddington rate (Sec.5). We conclude with Sec. 6 discussing future applications of HOLESOM.

2. SPECTRAL ENERGY DISTRIBUTIONS

Training the ML-powered HOLESOM to recognize and correctly classify the properties of MBHs requires a large library of ADAF SEDs. One method to obtain realistic ADAF SEDs is to execute a GRMHD simulation of a MBH of a given mass, and ray trace its spectral emission with codes such as `grMonty` (Dolence et al. 2009). However, this method is computationally expensive if a number $N \gg 1$ of training SEDs are required. In fact, to obtain a reliable spectrum, about 100 different GRMHD snapshots are typically necessary Dolence et al. (2009), with each snapshot demanding approximately half an hour of computational time on a single core. For our ML application, the number of required training SEDs is typically $N \sim 10^4$.

In order to obtain a large library of SEDs to develop HOLESOM, we then rely on analytical models, firstly developed by Mahadevan (1997) and further developed and coded by Pesce et al. (2021). This model describes self-similar ADAF, characterizing the local properties of the accreting gas based on parameters such as mass, accretion rate, radius, and viscosity parameters, among other variables. In this regime, the accreting gas forms a two-temperature, optically thin plasma where ions are at their virial temperature while electrons remain cooler. The pressure arises from both gas and magnetic contributions. The emission mechanisms include synchrotron radiation, inverse Compton scattering, and bremsstrahlung (Mahadevan 1997). This model calculates the spectral luminosity L_ν emitted by black holes of any mass, up to an Eddington ratio of $f_{\text{Edd}} = 10^{-1.7}$; the only two parameters required to generate the SED are the black hole mass M_\bullet and the Eddington ratio f_{Edd} .

To construct our SED library, we compute L_ν at 54 frequencies spanning from 5.0×10^9 to 1.9×10^{19} Hz, namely from 5 GHz in the radio band to 10 keV in the X-ray. We generated SEDs for MBHs with mass and Eddington ratio in the ranges $\log_{10}(M_\bullet/M_\odot) = [3,8]$ and $\log_{10} f_{\text{Edd}} = [-8,-2]$, respectively. Each range was divided into 140 logarithmic bins, thus obtaining a total of $140^2 = 19600$ spectra. From this data set, we removed a small set of outliers (i.e., $\sim 0.3\%$ of the initial distribution) because the resulting SED showed clear signs of numerical problems, which occurred typically for ex-

tremely low values of the Eddington ratio $f_{\text{Edd}} \sim 10^{-8}$. Hence, the final number of SEDs used to train our ML algorithm is 19535.

Figure 1 displays the general distribution of νL_ν in the radio (5 GHz) vs. the integrated X-ray luminosity (2 – 10 keV) for our SEDs. No strong correlation between radio and X-ray luminosity is evident for such a vast collection of black hole masses and Eddington ratios. However, the left panel, color-coded by $\log_{10} f_{\text{Edd}}$, shows that the X-ray luminosity increases as the Eddington ratio increases. In contrast, the right panel, color-coded by $\log_{10} M_\bullet$, shows that radio luminosity increases with black hole mass.

3. METHODS

In this Section, we first describe the ML algorithm underlying HOLESOM and its training process, followed by the methods employed to derive analytical equations in Sec.5.

3.1. Self-Organizing Maps

We develop HOLESOM on the basis of the ML algorithm named Self-Organizing Maps (SOMs) (Kohonen 1982). SOMs are a type of unsupervised artificial neural network (see, e.g., Baron 2019 for a review) that reduces a high-dimensional parameter space to a lower-dimensional representation while preserving the original topology. In this way, similar objects in the high-dimensional parameter space will be grouped in the final map, maintaining the intrinsic structure of the input data. In this study, we reduce the dimensionality to 2, as this choice facilitates visualization. We use the publicly-available code SOMPY¹ library (Moosavi et al. 2014a) to construct and train our SOM.

Each pixel of the 2D map is characterized by a weight vector corresponding to a position in the higher-dimensional parameter space of the input data, normalized to the unit variance with a mean of zero. The weight vectors are initialized through principal component analysis (PCA; Chatfield & Collins 1980) and then updated iteratively to minimize the Euclidean distance to the input data and reduce the quantization error.

3.1.1. Training and Visualization

In SOM algorithms, input features are individual attributes of the dataset that are fed into the SOM for analysis. These features define the higher-dimensional space, which the SOM reduces to the 2D grid. The input features of HOLESOM, which are given by different pho-

¹ <https://github.com/sevamoo/SOMPY>

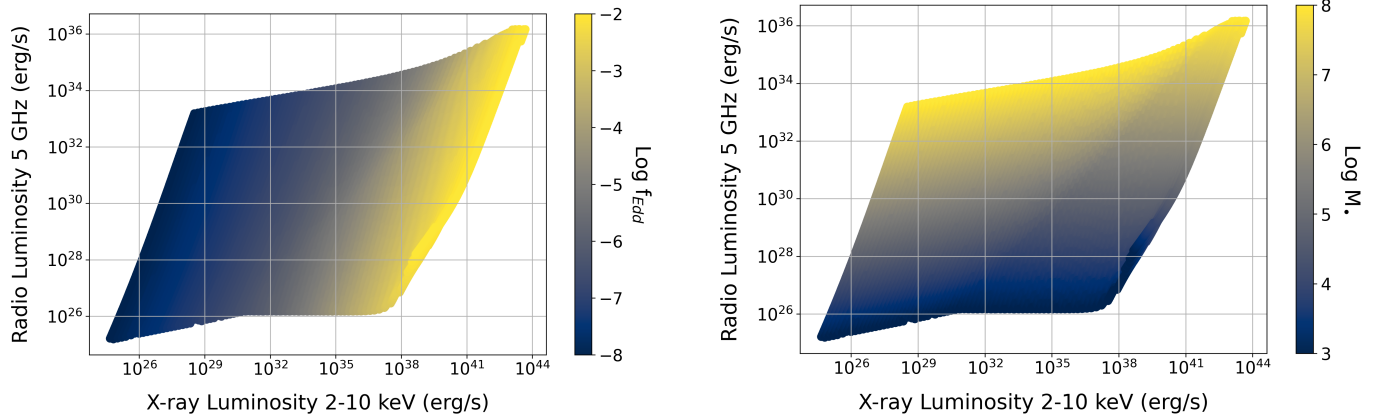


Figure 1. Luminosity at 5 GHz versus the integrated X-ray luminosity at 2 – 10 keV from our SED catalog, color-coded by f_{Edd} (left panel) and M_{\bullet} (right panel). These plots demonstrate that, while there is no evident correlation between radio and X-ray luminosity, the latter generally increases with f_{Edd} , while the former with M_{\bullet} .

tometric data points for a given source, are summarized in Table 1.

These input features were carefully selected among all the values of the luminosities νL_{ν} and all the possible SED slopes (see Section 2) to ensure homogeneous frequency coverage from radio to X-rays and strong correlation with M_{\bullet} and f_{Edd} . Specifically, we computed the distance correlation between M_{\bullet} and f_{Edd} with the luminosities as well as the SED slopes across all possible combinations (i.e., 1326) of two frequencies.

The size and geometry of our SOM are optimized for data clustering and performance, following the method described in Davidzon et al. (2019), resulting in a final map of 28×18 pixels. Black holes with similar SEDs are placed in the same or nearby pixels on the map. Since a given SED depends on its Eddington ratio and black hole mass, objects in the same pixel share similar SEDs (and, hence, similar f_{Edd} and M_{\bullet}).

For each pixel, we compute the median values of f_{Edd} and M_{\bullet} . The top panel of Fig. 2 shows the fully trained SOM color-coded by median $\log_{10} f_{\text{Edd}}$, with values smoothly increasing vertically from top to bottom. In contrast, median $\log_{10} M_{\bullet}$ values progressively increase leftwards, as shown by the shades of gray contours with values indicated in the color bar on the left.

The pixel distributions of M_{\bullet} and f_{Edd} are generally narrow, with σ_{STD} ranging between 0.03 – 0.09 dex for $\log_{10} M_{\bullet}$ and 0.02 – 0.08 dex for $\log_{10} f_{\text{Edd}}$. To demonstrate that the clustering process was successful, the bottom panel of Fig. 2 shows five median SEDs, along with their standard deviations, from five test pixels circled on the map in the top panel. These pixels represent different regimes of M_{\bullet} and f_{Edd} : (1) is high M_{\bullet} and low f_{Edd} , (2) is low M_{\bullet} and low f_{Edd} , (3) is intermediate M_{\bullet} and intermediate f_{Edd} , (4) is high M_{\bullet} and high f_{Edd} , (5) is low M_{\bullet} and high f_{Edd} . The shaded regions indicate

that the SEDs in each pixel are very well-constrained, with small deviations around the median.

Table 1. Summary of input features for the SOM algorithm.

Input Feature	Frequency (Hz)
Radio Luminosity	
5 GHz	5×10^9
50 GHz	5×10^{10}
230 GHz	2.3×10^{11}
X-ray Luminosity	
2-10 keV	$4.8 \times 10^{17} - 2.4 \times 10^{18}$
SED Slopes	
Radio (5-950 GHz)	$5 \times 10^9 - 9.5 \times 10^{11}$
Far-Infrared (316 - 25.5 μm)	$9.5 \times 10^{11} - 1.2 \times 10^{13}$
Mid-Infrared (25.5 - 8.6 μm)	$1.2 \times 10^{13} - 3.5 \times 10^{13}$
Near-Infrared (8.6 - 1.5 μm)	$3.5 \times 10^{13} - 2 \times 10^{14}$
Optical (1.5 - 0.4 μm)	$2 \times 10^{14} - 7.7 \times 10^{14}$
UV (0.4 - 0.17 μm)	$7.7 \times 10^{14} - 1.8 \times 10^{15}$

3.2. Polynomial and Symbolic Regressions

In this Section, we describe the two regression techniques employed to derive the analytical relations presented in Sec. 5: polynomial and symbolic regression.

We first employ polynomial regression to capture the relationships between M_{\bullet} and the radio luminosity at 5 GHz, and between f_{Edd} and the X-ray luminosity at 2-10 KeV. Polynomial regression fits the data to a polynomial function of a given degree, allowing for the modeling of non-linear trends without increasing the complexity of the model. We used the `numpy.polyfit` function from the Numpy library for this task and chose a

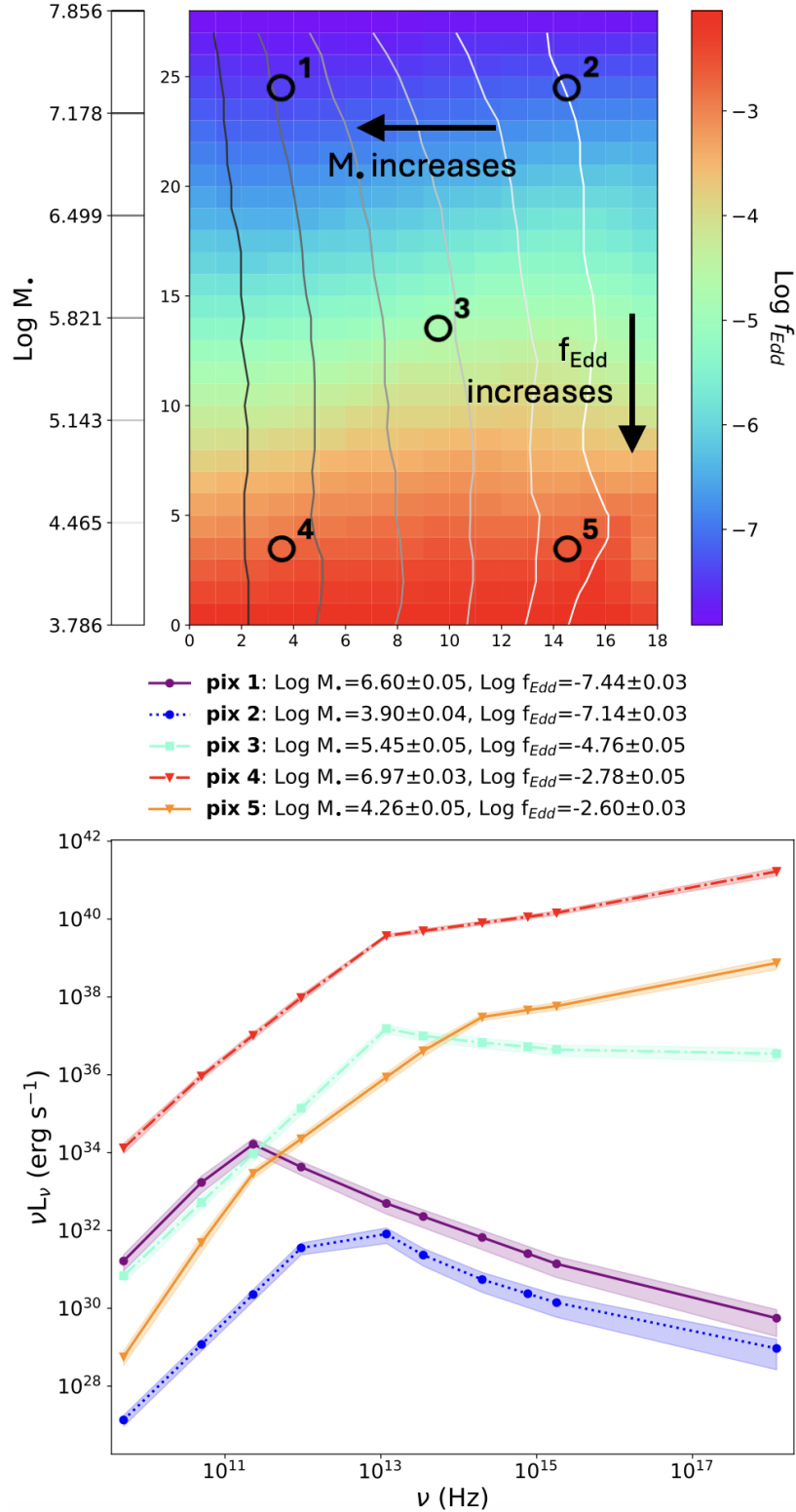


Figure 2. *Top panel:* Trained SOM color-coded by $\log_{10} f_{\text{Edd}}$. The different shades of gray contours indicate $\log_{10} M_{\bullet}$ values, as shown in the left color bar. The open circles represent five pixels (pixel 1 = [3,24], pixel 2 = [14,24], pixel 3 = [9,13], pixel 4 = [3,3], pixel 5 = [14,3]), covering different combinations of M_{\bullet} and f_{Edd} . From these pixels, we select test MBHs for the analysis of Sec. 4. *Bottom panel:* SEDs of MBHs located in the five test pixels. The shaded regions indicate the standard deviation of the spectral luminosity in that pixel, whose median values for $\log_{10} M_{\bullet}$ (in units of M_{\odot}) and $\log_{10} f_{\text{Edd}}$ are reported in the legend with the corresponding standard deviation of their distribution in their pixel.

second-degree polynomial fit. This choice was based on the observation that higher-degree polynomials did not significantly improve the fit, and the data distributions did not exhibit complex behaviors.

However, we employ symbolic regression for more complex relationships where a polynomial fit would be insufficient. This machine-learning technique finds mathematical equations to describe data by combining basic operators like addition and multiplication. Unlike polynomial regression, which fits data to a predefined function, symbolic regression explores a vast space of possible equations to identify the one that best captures the relationships in the data. We used the PySR² library Cranmer (2023), which employs an evolutionary algorithm inspired by natural selection. The algorithm starts with a group of randomly generated equations (i.e., the “individuals”) and gradually improves them. Each step selects the best-performing equations based on how well they fit the data, applies random changes (the “mutations”) to generate new equations, and replaces weaker ones with stronger ones. This process repeats many times, evolving the equations toward better solutions.

For our training, we employ a representative subset of 1000 randomly selected objects and configured the model with `populations=100`, allowing for the exploration of a diverse set of solutions by evolving multiple independent groups of candidate equations. We set `niterations=50` to allow enough iterations for each population to evolve through mutation and selection. Additionally, we allow basic binary operators $\{+, -, \times, /\}$ and unary operators $\{\text{square, cube, exp}\}$ during the symbolic regression.

4. RESULTS

In this Section, we apply the ML method described thus far, adopting a progressive approach. First, we test how well we can constrain the main physical parameters of a putative source if data is available only in a very limited set of frequencies (Sec. 4.1). This, of course, will be the case with any real-world application. Second, we test HOLESOM with the archetypal example of an ADAF MBH: Sgr A* (Sec. 4.2). In doing this, we highlight why this source is peculiar and possibly not representative of the majority of sources to which our methodology can be applied. Then, in Sec. 4.3 we show that the MBHs accreting in ADAF mode can be effectively disentangled from stellar-mass accretors (e.g., stellar-mass black holes, neutron stars, pulsars).

4.1. Evaluating f_{Edd} and M_{\bullet} ranges with limited data

We now test the fully-trained SOM to investigate how it performs in real-world scenarios. In an ideal situation, a given source possesses a large wealth of multi-wavelength data, spanning from radio to X-ray. In most cases, however, only a limited amount of data can be securely associated with a given source, with a number of data points that is typically lower than the 10 input features with which our code was trained. The relevant question is: how well the physical parameters of the MBH can be constrained if one or more multi-wavelength data points are missing?

At this stage, it is important to understand that HOLESOM is a tool whose main goals are to identify slowly-accreting MBHs candidates and provide an *estimate* of their physical parameters, based on very limited photometric data. Once candidates are identified, additional follow-up photometric data will improve our estimate, while spectroscopy will ultimately investigate their nature in detail.

Hence, our goal is to investigate whether, with scarce data we can: (i) correctly classify the mass category of a MBH and (ii) constrain its Eddington ratio within the upper end of the ADAF range (i.e., $f_{\text{Edd}} \sim 10^{-2} - 10^{-3}$), or at severely low rates (i.e., $f_{\text{Edd}} \ll 10^{-3}$). We first discuss the ideal scenario with no missing observations. Next, we explain how to estimate parameters when data is missing, beginning with the case of a single missing photometric point and concluding with scenarios of multiple missing observations.

We take one test MBH from each of the five test pixels described in Sec. 3.1. When all input features are available, we assign the median values of f_{Edd} and M_{\bullet} from the corresponding pixel to the test MBH. The uncertainty is given by the standard deviation of these parameter distributions within the pixel. The accuracy of this approach is illustrated in Fig. 3 for “Pixel 4”, showing that the estimated parameters are very accurate when no photometry information is missing.

For a more realistic scenario, we remove one photometric band at a time. We then recover that specific missing information following the method detailed in La Torre et al. (2024), to which the interested reader is referred to. In summary, this method consists of randomly drawing 5000 new values of the missing feature from the distribution of the rest of the training sample, under the assumption that the missing value falls within the same distribution as the sample and it is not a peculiar case. Then, given the new set of input features, we project the MBH onto the SOM, creating a 2D likelihood surface of the possible pixel occupied by the MBH. From that, we extract the probability distribution function of

² A description of PySR is available at this [link](#).

f_{Edd} and M_{\bullet} for that MBH, given the recovered missing data.

As an example, Figure 3 shows the ranges of f_{Edd} (left panel) and M_{\bullet} (right panel) for recovered missing data of a test MBH selected from the test pixel 4 (see Figure 2). Results for the other test pixels are reported in Appendix A. Here, we begin by discussing the process of constraining f_{Edd} and then proceed to M_{\bullet} , starting with a single missing observation and then addressing multiple missing observations.

For f_{Edd} , we observe that the ranges are consistent with the true value, especially in the upper sub-Eddington regime around 10^{-3} - 10^{-2} (i.e., Figure 9 in the Appendix), where f_{Edd} is mainly affected by IR, optical, UV, and X-ray observations. This result also holds in the low end of f_{Edd} around 10^{-8} - $10^{-7} M_{\odot} \text{yr}^{-1}$ (i.e., the top two panels in Figure 8 in the Appendix). Even with missing data, we can constrain f_{Edd} to be in the upper or lower ranges in the sub-Eddington regime. This result slightly differs for a MBH in an intermediate sub-Eddington regime (i.e., $\sim 10^{-5}$), as shown in the bottom row of Figure 8, for a MBH in pixel 3. Here, radio observations start to affect the process of constraining f_{Edd} ; specifically, recovering the missing luminosity at 950 GHz would place this object in a deeper sub-Eddington regime.

Recovering missing observations yields consistent ranges of M_{\bullet} with the true values for cases at the high end of the black hole mass (i.e., $\sim 10^7 M_{\odot}$). Unlike f_{Edd} , radio and MIR luminosities mainly influence the mass range. This pattern also holds in the opposite regime, i.e., at the low mass end (pixel 2 and 5 in Figure 8), where recovering missing observations still yields consistent mass ranges compared to the true value. However, missing luminosity at 5 GHz and/or at $8.6 \mu\text{m}$ could result in mass regimes differing by $\sim 1 - 2$ orders of magnitude. For the intermediate mass case (pixel 3), the mass ranges are consistent with the true value within the margin of error.

While the previous results focused on recovering a single missing observation, we now examine the results when multiple missing observations are recovered. The bottom rows of Figure 3 show the ranges of f_{Edd} and M_{\bullet} for a test MBH from pixel 4 when several observations (from X-ray to IR) are missing. For results from the other test pixels, refer to Appendix A. The worst case among the five test MBHs is represented by black holes with very low f_{Edd} (i.e., $< 10^{-7}$; see pixel 1 and 2). Conversely, for larger f_{Edd} , this combination of missing observations produces f_{Edd} ranges consistent with the true value within the margin of error, even though these ranges can be broad. In essence, constraining f_{Edd}

within a narrow range is challenging when X-ray, UV, optical, and IR are all missing. However, in this scenario, M_{\bullet} ranges remain consistent across all five test black holes (Figure 11). As previously mentioned, M_{\bullet} estimation is not significantly affected by X-ray, UV, optical, and IR observations.

In conclusion, in the ideal scenario of no missing data (i.e., ~ 10 photometric data points), f_{Edd} and M_{\bullet} are estimated with high accuracy. In case of missing X-ray data or, more generally, a single-band observation, HOLESOM remains effective in correctly classifying MBHs within reasonable mass and accreting ADAF ranges. In the case of numerous missing data points, the uncertainty is higher, but HOLESOM still remains effective in correctly identifying a slowly-accreting MBH and approximating its mass and Eddington ratio.

4.2. The Golden Test: Sgr A*

We test HOLESOM on the archetypal case of a MBH accreting in ADAF mode: Sgr A*. Although this MBH represents a perfect test case for our approach, we highlight two significant differences between Sgr A* and the typical MBH that we will target with our code: First, the mass of Sgr A*, and, to some extent, its Eddington ratio, are known from a variety of independent observations, starting from the dynamics of stars in its immediate vicinity (see, e.g., Ghez et al. 2008) to recent measurements by the Event Horizon Telescope (Event Horizon Telescope Collaboration et al. 2022). The mass is $M_{\bullet} = 4.0_{-0.6}^{+1.1} \times 10^6 M_{\odot}$, with an Eddington ratio of $\sim 10^{-7}$. Our methodology, based on only a few photometric data points, aims at broadly characterizing the mass and accretion regime of the MBH, and cannot compete with such accurate measurements. However, it is instructive to check whether our estimate is compatible with the true value for Sgr A*. Second, Sgr A* is located in the Galactic center, and characterized by heavy obscuration by interstellar dust (see, e.g., Fritz et al. 2016), which makes observations in the optical and UV practically impossible. Targeting extragalactic MBHs, or off-centered wandering MBHs in the Milky Way, will avoid this issue. However, for this test, we feed the code only with radio, sub-millimeters, and X-ray data points for Sgr A*.

Radio observations at 5, 50, and 950 GHz are taken from Markoff et al. (2001); Yuan et al. (2003); Dodds-Eden et al. (2009); at 230 GHz from Bower et al. (2019), and the X-ray luminosity of Sgr A* in its quiescent state is from Baganoff et al. (2003). The input features used are the same as those in Table 1, with the exception that we use only the SED slope between 5 and 950 GHz, and use a new slope between radio (950 GHz) and X-ray.

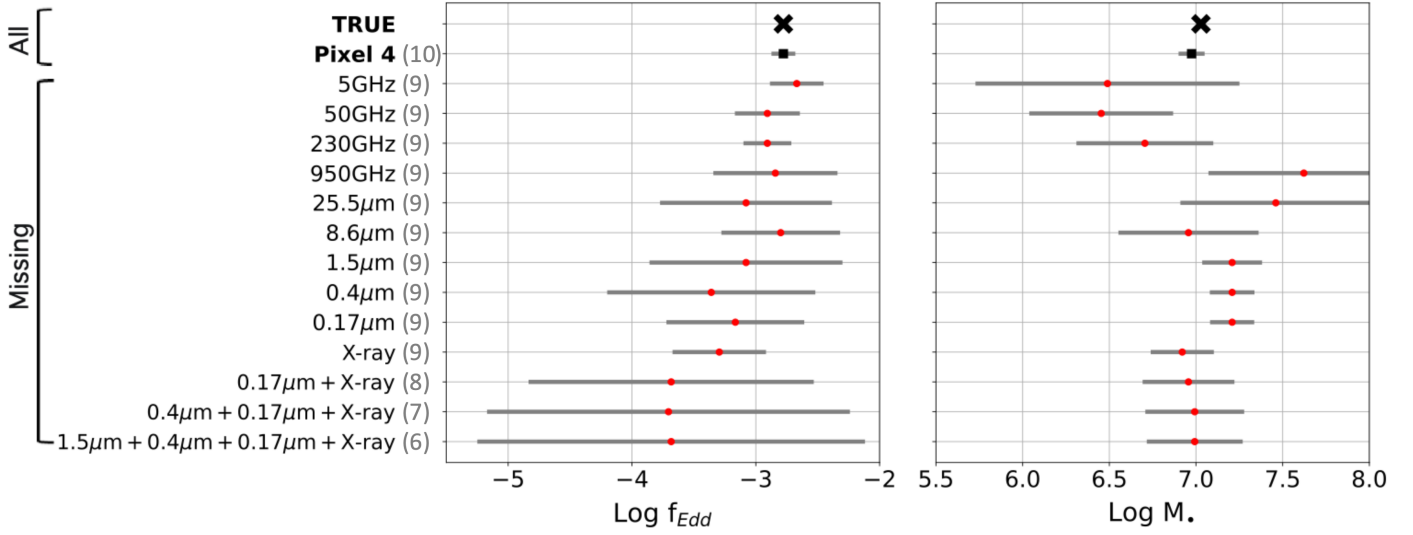


Figure 3. For a test MBH located in *pixel 4*, we illustrate the values of $\text{Log } f_{\text{Edd}}$ (left) and M_* (right) estimated with HOLESOM, in various cases of data availability. The numbers in parenthesis indicate how many of the 10 bands are available. In the top rows, labeled ‘All’, we show the true values of the test MBH, marked by a black cross. The black square indicates, when all bands are available, the median of the parameter distribution within *pixel 4*, with the grey line showing the standard deviation of that distribution. In the lower rows, labeled ‘Missing’, we show the parameter ranges after recovering one or multiple missing observations (Section 4.1). In these cases, the red circle marks the peak of the probability distribution function for the estimated parameter after recovering missing data, while the grey line again represents the standard deviation. Additional test MBHs from other pixels are shown in the Appendix A.

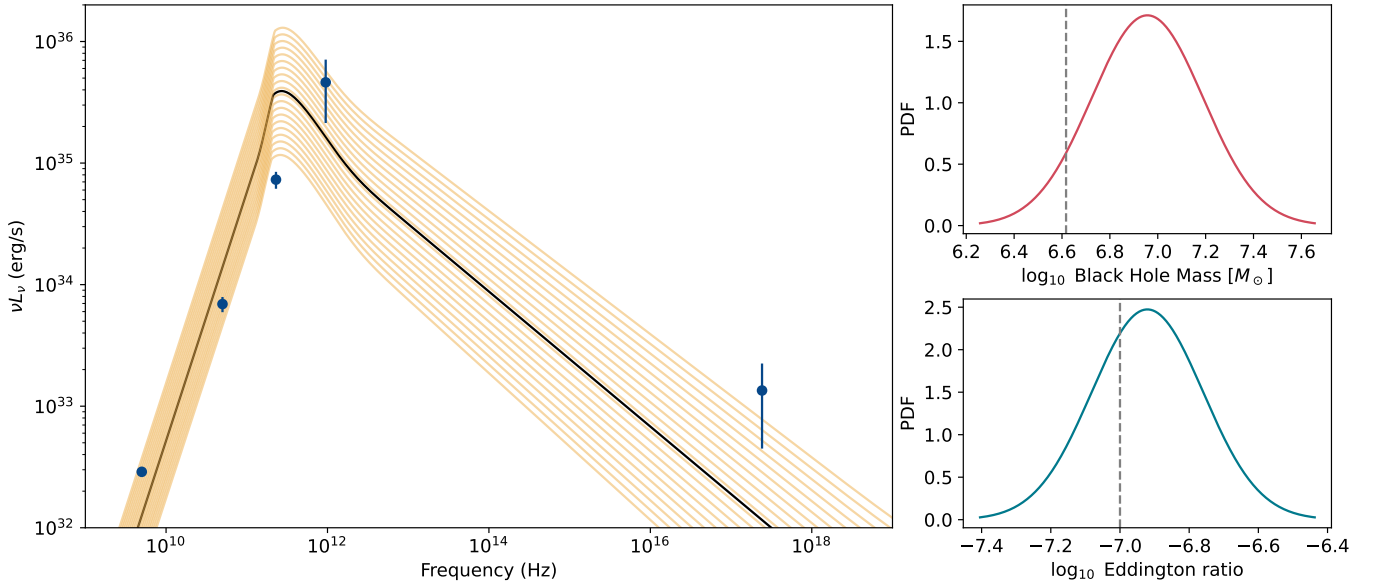


Figure 4. Test case for Sgr A*. The left panel shows the SEDs selected by our code as the ones that best describe the data, shown in blue with their 1σ error bars. The black line shows our median SED, while the yellow region displays its 3σ uncertainty. For this test, we use only data from the radio, sub-millimeters, far infrared, and X-ray bands. The right panels show the inferred distributions for the black hole mass (top) and Eddington ratio (bottom), with their true values indicated by dashed lines.

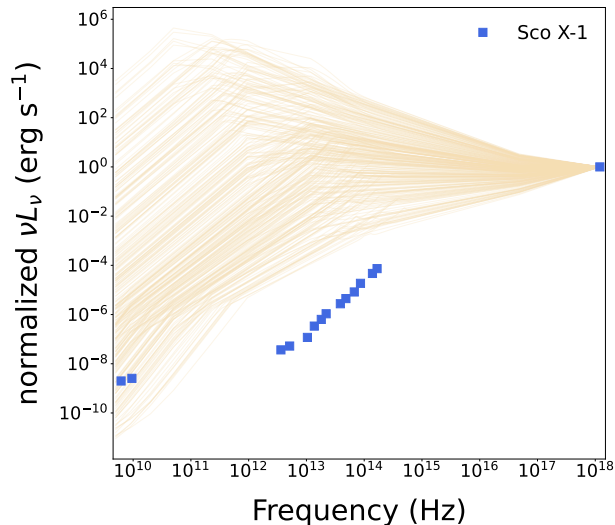


Figure 5. Comparison between 300 models for MBH SEDs (orange lines), randomly drawn from the training set to cover all the physical parameter space, and the photometry for neutron star Sco X-1 (blue squares). Luminosities are normalized to the X-ray value.

This additional slope helps track the synchrotron peak, as no information is employed for wavelengths in between. We also include photometric errors following the approach described in (La Torre et al. 2024). We generate 50 new input datasets by drawing new random luminosities from a Gaussian distribution centered on the true luminosity with a width equal to the error. Each of these 50 datasets is then projected onto the trained SOM. As described in Section 4, the ranges of M_{\bullet} and f_{Edd} are determined from the 2D likelihood surface of these datasets on the SOM. Figure 4 shows the probability distribution function (PDF) of the derived M_{\bullet} and f_{Edd} , compared to the true values for Sgr A*, and the corresponding SED models, which are consistent with the observed photometric points and their errors.

4.3. Disentangling MBHs from Stellar-Mass Objects

Figure 1 suggests that slowly-accreting MBHs do not generally follow the well-known relations between radio and X-ray luminosities typical of stellar-mass compact objects, where $L_R \propto \sqrt{L_X}$ Gallo et al. (2003, 2018); Gusinskaia et al. (2020). Furthermore, as shown for the neutron star SCO X-1³ in Figure 5, the two populations of MBHs and stellar-mass compact objects have remarkably different SEDs.

We test whether HOLESOM can *filter out* stellar-mass compact objects, as they would not be projected on the same map trained with SEDs compatible with the MBH

population. In principle, this applies when a test stellar-mass BH has complete photometric data across the employed feature set. In practice, the challenge arises with missing data. While in the previous sections we “filled-in” missing MHB data using luminosity or SED slope distributions from the MBH training set, now such distributions for the stellar-mass BH population are not available. Using MBH distributions to fill in missing stellar-mass BH data would make their SEDs more similar to those of MBHs, potentially blurring the distinction between the two populations.

We test this effect by projecting Sco X-1 onto our SOM. Of the 10 input features used for training (Table 1), 6 are missing. We only have the radio luminosity at 5 GHz, the X-ray luminosity, and the IR luminosities at 25.5, 8.6, and 1.5 μm , i.e., 5 bands out of the 10 needed to construct the full feature set. Although we recover missing data using MBH priors (aware that this might make Sco X-1’s SED more similar to MBHs), Sco X-1 still lands at the edge of the map, specifically in pixel [18,0], which corresponding to $\log f_{\text{Edd}} \sim -2$ and $\log M_{\bullet} < 3.786$, values consistent with stellar-mass objects. This indicates that even with data recovering, the differences in SEDs are sufficient for HOLESOM to identify Sco X-1 as an outlier, which is typically placed at the edges of the map (see, e.g., Davidzon et al. 2019).

In conclusion, HOLESOM effectively identifies and classifies MBHs based on their SEDs, projecting them into pixels that reflect their SEDs and parameters. In contrast, objects with significantly different SEDs, like stellar-mass BHs, are typically placed outside the map or at the edges, indicating they are outliers while still yielding parameters consistent with low masses and accretion closer to the Eddington limit.

5. ANALYTICAL RELATIONS

Unlike stellar-mass BHs, which follow reasonably tight relations between radio and X-ray luminosities (see, e.g., Gallo et al. 2003), slowly-accreting MBHs do not exhibit such a strong correlation, as visually illustrated in Fig. 1. However, we observe that these luminosities depend on f_{Edd} and M_{\bullet} . These insights drive us to seek analytical expressions tailored for slowly-accreting MBHs in a wide range of black hole masses and Eddington ratios. In the following, we present only those relations that effectively balance complexity and accuracy.

In the top panel of Figure 6, we present the relationship between M_{\bullet} and radio luminosity at 5 GHz, fitted using polynomial regression. The resulting equation is expressed as:

$$\ell_m = \alpha_1 \ell_r^2 + \beta_1 \ell_r + \gamma_1 \quad (2)$$

³ The photometry for Sco X-1 was retrieved from this link.

where ℓ_m indicates $\text{Log}(M_\bullet)$, ℓ_r is the logarithm of the radio luminosity at 5 GHz, α_1 , β_1 , and γ_1 are constants whose values are reported in Table 2. In the the bottom panel of Fig.6, we show the equivalent relation between f_{Edd} and the X-ray luminosity:

$$\ell_f = \alpha_2 \ell_X^2 + \beta_2 \ell_X + \gamma_2 \quad (3)$$

where ℓ_f indicates $\text{Log}(f_{\text{Edd}})$, ℓ_X is the logarithm of the integrated X-ray luminosity at 2-10KeV. The values of the constants α_2 , β_2 , and γ_2 are also listed in Table 2.

However, Figure 1 shows that, at fixed X-ray lumi-

Table 2. Constants used in the equations in Sec.5.

$M_\bullet = f(L_{5\text{GHz}})$ (eq. 2)	$f_{\text{Edd}} = f(L_X)$ (eq. 3)	$L_{5\text{GHz}} = f(M_\bullet, L_X)$ (eq. 4)
$\alpha_1 = -0.0081$	$\alpha_2 = 0.0077$	$\alpha_3 = 0.0220$
$\beta_1 = 1.0367$	$\beta_2 = -0.1442$	$\beta_3 = 0.0404$
$\gamma_1 = -18.5593$	$\gamma_2 = -9.6431$	$\gamma_3 = -0.0220$
		$\delta_3 = 1.0287$
		$\epsilon = 19.8177$

osity, a source can exhibit either low or high radio luminosity, with the exception of very low and very high ends of the X-ray luminosity. This distribution is too complex for simple linear or polynomial models. Here, we turn to symbolic regression to capture $L_r = f(L_X, f_{\text{Edd}})$.

The best equation resulting from symbolic regression is:

$$\ell_r = (\alpha_3 \ell_m + \beta_3) \ell_X + (\gamma_3 \ell_m + \delta_3) \ell_m + \epsilon \quad (4)$$

with the constants α_3 , β_3 , γ_3 , δ_3 , and ϵ reported in Table 2. As shown in Figure 7, the predicted radio luminosity closely matches the true values, except for a few points in the $10^{27} - 10^{29}$ erg/s range. This is due to the abrupt decrease of M_\bullet at X-ray luminosity around $10^{38} - 10^{39}$ erg/s, as seen in Fig. 1. We quantify the goodness of our prediction by computing the root mean square error (RMSE) and the mean absolute error (MAE), which are reported in Fig. 7.

6. CONCLUSIONS

Detecting MBHs accreting at extremely low rates in radiatively inefficient modes remains a significant challenge in astrophysics. These objects, which are easily confused/contaminated with other classes of sources, require advanced techniques for accurate identification and characterization. In this paper, we introduced HOLESOM, a ML tool based on the SOM algorithm.

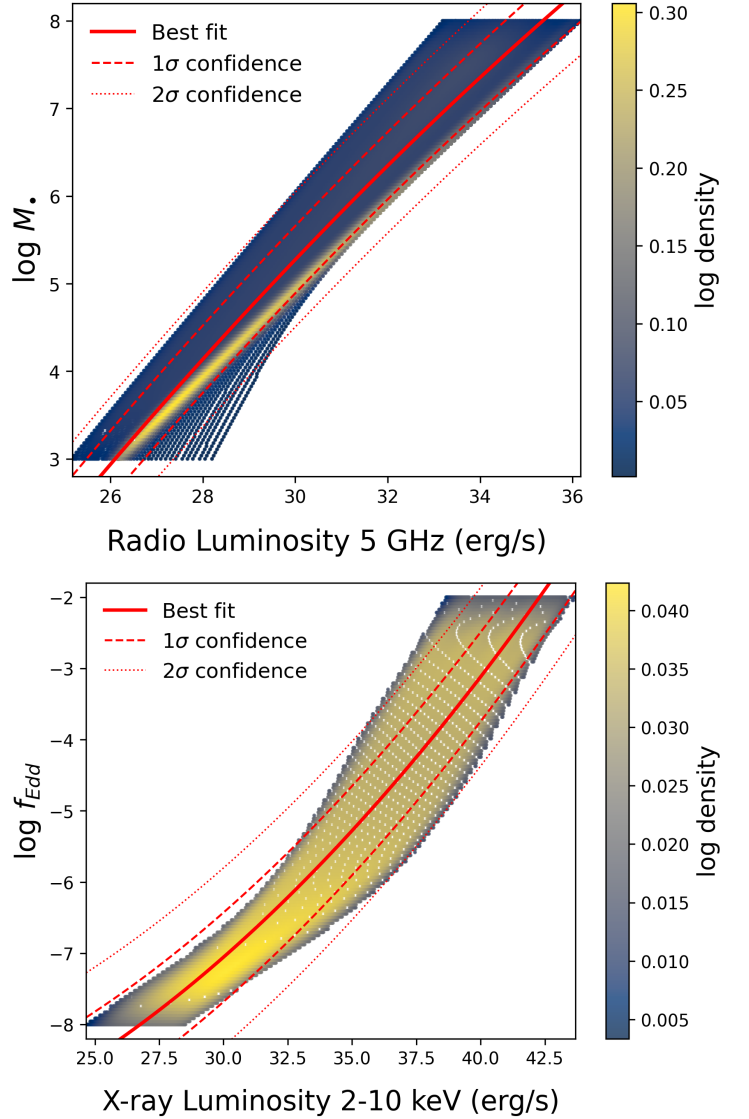


Figure 6. *Top:* Black hole mass [M_\odot] versus radio luminosity at 5 GHz, in units of erg/s. The red solid line represents the best fit of the distribution given by equation 2. The red dashed and dotted lines represent the 1σ and 2σ confidence levels.

Bottom: Eddington ratio versus luminosity in X-ray in erg/s. The red solid line and dashed and dotted lines are the same as in the top panel.

Trained with $\sim 20,000$ analytically-derived SEDs for ADAF accreting MBHs, HOLESOM (i) automatically identifies and separates MBHs accreting in ADAF mode from other classes of objects, and (ii) efficiently characterize their physical properties, even with scarce data. We also used polynomial and symbolic regression to derive analytical relationships between radio/X-ray luminosities and black hole mass and Eddington ratio, pro-

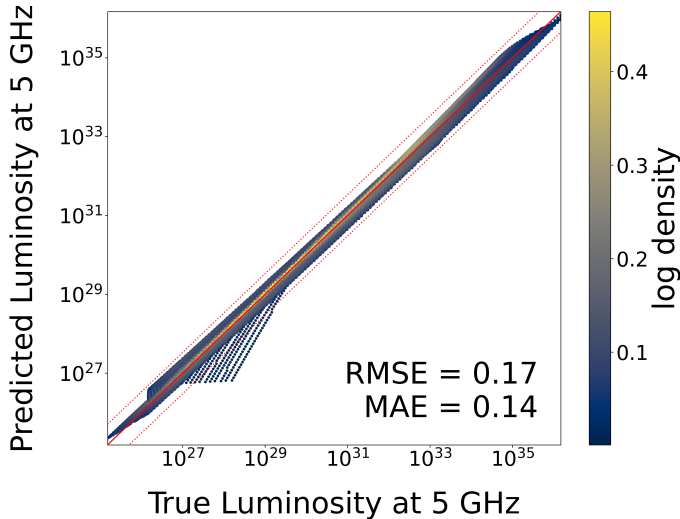


Figure 7. Comparison between the true radio luminosity at 5 GHz and the predicted values as a function of X-ray luminosity and M_{\bullet} , as inferred from Eq. 4. The solid red line represents the 1:1 correlation, while the dotted lines indicate the 3σ confidence level. The root mean square error and mean absolute error metrics are shown in the bottom-right corner.

viding additional insights into the behavior of MBHs radiating in ADAF mode.

A key result of this work is HOLESOM’s ability to estimate mass and Eddington ratio ranges of MBHs with high accuracy, even in the presence of missing photometric data, which are recovered following La Torre et al. (2024). As expected, the process becomes more challenging when the available data is very scarce, particularly for MBHs accreting at very low Eddington ratios. In such cases, the accuracy of the mass and Eddington ratio estimates diminishes, but they are still consistent with their true values within uncertainties in the majority of cases. This highlights the importance of adding multi-wavelength data to improve the characterization of these objects. However, we demonstrated the robustness of our method by applying the model to the real-world case of Sgr A*, where we retrieve distributions

of M_{\bullet} and f_{Edd} that were in excellent agreement with known values.

We also showed that a promising aspect of HOLESOM is its ability to disentangle the photometric signatures of MBHs from those of stellar-mass BHs (e.g., X-ray binaries) in the same dataset. By projecting objects onto the trained SOM, MBHs are placed in regions corresponding to their expected parameter values, while objects with significantly different SEDs, such as stellar-mass BHs, are typically identified as outliers, assigned to the edges of the map, or not projected onto the map at all.

In conclusion, HOLESOM provides a versatile and scalable framework for identifying and characterizing MBHs based on their SEDs. The usefulness of this method will become even more evident with large, multiwavelength, low- z datasets. Once MBH candidates are identified in these surveys, additional multi-wavelength data will progressively hone in on the object’s physical properties, optimizing the effectiveness of HOLESOM and minimizing the impact of multiple missing photometric bands. As these surveys continue to grow, the ability to automatically identify MBHs and estimate their properties will be invaluable for advancing our understanding of the role these objects play in the evolution of galaxies.

Acknowledgments: V.L.T. acknowledges support from the Smithsonian Astrophysical Observatory Visiting Fellowship, and the Kathryn A. McCarthy Graduate Fellowship in Physics administered by Tufts University. F.P. acknowledges support from a Clay Fellowship administered by the Smithsonian Astrophysical Observatory. This work was also supported by the Black Hole Initiative at Harvard University, funded by grants from the John Templeton Foundation and the Gordon and Betty Moore Foundation. This work used the FASRC cluster computer at Harvard University.

Software: SOMPY (Moosavi et al. 2014b), PYSR (Cramer 2023), `numpy.polyfit`.

REFERENCES

- Abramowicz, M. A., Chen, X., Kato, S., Lasota, J.-P., & Regev, O. 1995, *ApJL*, 438, L37, doi: [10.1086/187709](https://doi.org/10.1086/187709)
- Ananna, T. T., Salvato, M., LaMassa, S., et al. 2017, *ApJ*, 850, 66, doi: [10.3847/1538-4357/aa937d](https://doi.org/10.3847/1538-4357/aa937d)
- Ananna, T. T., Weigel, A. K., Trakhtenbrot, B., et al. 2022, *ApJS*, 261, 9, doi: [10.3847/1538-4365/ac5b64](https://doi.org/10.3847/1538-4365/ac5b64)
- Baganoff, F. K., Maeda, Y., Morris, M., et al. 2003, *ApJ*, 591, 891, doi: [10.1086/375145](https://doi.org/10.1086/375145)
- Baldassare, V. F., Reines, A. E., Gallo, E., & Greene, J. E. 2015, *ApJ*, 809, doi: [10.1088/2041-8205/809/1/L14](https://doi.org/10.1088/2041-8205/809/1/L14)
- Bardeen, J. M. 1970, *Nature*, 226, 64, doi: [10.1038/226064a0](https://doi.org/10.1038/226064a0)
- Baron, D. 2019, arXiv e-prints, arXiv:1904.07248, doi: [10.48550/arXiv.1904.07248](https://doi.org/10.48550/arXiv.1904.07248)
- Blandford, R. D., & Znajek, R. L. 1977, *MNRAS*, 179, 433, doi: [10.1093/mnras/179.3.433](https://doi.org/10.1093/mnras/179.3.433)

- Bower, G. C., Dexter, J., Asada, K., et al. 2019, *ApJL*, 881, L2, doi: [10.3847/2041-8213/ab3397](https://doi.org/10.3847/2041-8213/ab3397)
- Cappelluti, N., Pacucci, F., & Hasinger, G. 2024, arXiv e-prints, arXiv:2406.07602, doi: [10.48550/arXiv.2406.07602](https://doi.org/10.48550/arXiv.2406.07602)
- Chatfield, C., & Collins, A. J. 1980, Chapman & Hall, doi: [10.1007/978-1-4899-3184-9](https://doi.org/10.1007/978-1-4899-3184-9)
- Cranmer, M. 2023, Interpretable Machine Learning for Science with PySR and SymbolicRegression.jl. <https://arxiv.org/abs/2305.01582>
- Davidzon, I., Laigle, C., Capak, P. L., et al. 2019, *Monthly Notices of the Royal Astronomical Society*, 489, 4817, doi: [10.1093/mnras/stz2486](https://doi.org/10.1093/mnras/stz2486)
- Davidzon, I., Laigle, C., Capak, P. L., et al. 2019, *MNRAS*, 489, 4817, doi: [10.1093/mnras/stz2486](https://doi.org/10.1093/mnras/stz2486)
- Di Matteo, T., Ni, Y., Chen, N., et al. 2023, *MNRAS*, 525, 1479, doi: [10.1093/mnras/stad2198](https://doi.org/10.1093/mnras/stad2198)
- Di Matteo, T., Springel, V., & Hernquist, L. 2005, *Nature*, 433, 604, doi: [10.1038/nature03335](https://doi.org/10.1038/nature03335)
- Dodds-Eden, K., Porquet, D., Trap, G., et al. 2009, *The Astrophysical Journal*, 698, 676, doi: [10.1088/0004-637X/698/1/676](https://doi.org/10.1088/0004-637X/698/1/676)
- Dolence, J. C., Gammie, C. F., Mościbrodzka, M., & Leung, P. K. 2009, *ApJS*, 184, 387, doi: [10.1088/0067-0049/184/2/387](https://doi.org/10.1088/0067-0049/184/2/387)
- Elvis, M., Wilkes, B. J., McDowell, J. C., et al. 1994, *ApJS*, 95, 1, doi: [10.1086/192093](https://doi.org/10.1086/192093)
- Event Horizon Telescope Collaboration, Akiyama, K., Alberdi, A., et al. 2022, *ApJL*, 930, L12, doi: [10.3847/2041-8213/ac6674](https://doi.org/10.3847/2041-8213/ac6674)
- Ferrarese, L., & Merritt, D. 2000, *ApJL*, 539, L9, doi: [10.1086/312838](https://doi.org/10.1086/312838)
- Fritz, T. K., Chatzopoulos, S., Gerhard, O., et al. 2016, *ApJ*, 821, 44, doi: [10.3847/0004-637X/821/1/44](https://doi.org/10.3847/0004-637X/821/1/44)
- Gallo, E., Degenaar, N., & van den Eijnden, J. 2018, *MNRAS*, 478, L132, doi: [10.1093/mnrasl/sly083](https://doi.org/10.1093/mnrasl/sly083)
- Gallo, E., Fender, R. P., & Pooley, G. G. 2003, *MNRAS*, 344, 60, doi: [10.1046/j.1365-8711.2003.06791.x](https://doi.org/10.1046/j.1365-8711.2003.06791.x)
- Gebhardt, K., Bender, R., Bower, G., et al. 2000, *ApJL*, 539, L13, doi: [10.1086/312840](https://doi.org/10.1086/312840)
- Genzel, R., Pichon, C., Eckart, A., Gerhard, O. E., & Ott, T. 2000, *MNRAS*, 317, 348, doi: [10.1046/j.1365-8711.2000.03582.x](https://doi.org/10.1046/j.1365-8711.2000.03582.x)
- Ghez, A. M., Morris, M., Becklin, E. E., Tanner, A., & Kremenek, T. 2000, *Nature*, 407, 349, doi: [10.1038/35030032](https://doi.org/10.1038/35030032)
- Ghez, A. M., Salim, S., Weinberg, N. N., et al. 2008, *The Astrophysical Journal*, 689, 1044, doi: [10.1086/592738](https://doi.org/10.1086/592738)
- Greene, J. E., Strader, J., & Ho, L. C. 2020, *ARA&A*, 58, 257, doi: [10.1146/annurev-astro-032620-021835](https://doi.org/10.1146/annurev-astro-032620-021835)
- Gusinskaia, N. V., Russell, T. D., Hessels, J. W. T., et al. 2020, *MNRAS*, 492, 1091, doi: [10.1093/mnras/stz3460](https://doi.org/10.1093/mnras/stz3460)
- Haardt, F., & Maraschi, L. 1991, *ApJL*, 380, L51, doi: [10.1086/186171](https://doi.org/10.1086/186171)
- Kohonen, T. 1982, *Biological Cybernetics*, 43, 59, doi: [10.1007/BF00337288](https://doi.org/10.1007/BF00337288)
- Kormendy, J., & Ho, L. C. 2013, *Annual Review of Astronomy and Astrophysics*, 51, 511, doi: [10.1146/annurev-astro-082708-101811](https://doi.org/10.1146/annurev-astro-082708-101811)
- Koss, M. J., Ricci, C., Trakhtenbrot, B., et al. 2022, *ApJS*, 261, 2, doi: [10.3847/1538-4365/ac6c05](https://doi.org/10.3847/1538-4365/ac6c05)
- La Torre, V., Sajina, A., Goulding, A. D., et al. 2024, arXiv e-prints, arXiv:2403.18888, doi: [10.48550/arXiv.2403.18888](https://doi.org/10.48550/arXiv.2403.18888)
- Magorrian, J., Tremaine, S., Richstone, D., et al. 1998, *AJ*, 115, 2285, doi: [10.1086/300353](https://doi.org/10.1086/300353)
- Mahadevan, R. 1997, *ApJ*, 477, 585, doi: [10.1086/303727](https://doi.org/10.1086/303727)
- Maiolino, R., Scholtz, J., Witstok, J., et al. 2023, arXiv e-prints, arXiv:2305.12492, doi: [10.48550/arXiv.2305.12492](https://doi.org/10.48550/arXiv.2305.12492)
- Markoff, S., Falcke, H., Yuan, F., & Biermann, P. L. 2001, *A&A*, 379, L13, doi: [10.1051/0004-6361:20011346](https://doi.org/10.1051/0004-6361:20011346)
- Molina, M., Reines, A. E., Latimer, L. J., Baldassare, V., & Salehirad, S. 2021, *ApJ*, 922, 155, doi: [10.3847/1538-4357/ac1ffa](https://doi.org/10.3847/1538-4357/ac1ffa)
- Moosavi, V., Packmann, S., & Vallés, I. 2014a —. 2014b, *SOMPY: A Python Library for Self Organizing Map (SOM)*
- Mullaney, J. R., Alexander, D. M., Goulding, A. D., & Hickox, R. C. 2011, *MNRAS*, 414, 1082, doi: [10.1111/j.1365-2966.2011.18448.x](https://doi.org/10.1111/j.1365-2966.2011.18448.x)
- Narayan, R., Chael, A., Chatterjee, K., Ricarte, A., & Curd, B. 2022, *MNRAS*, 511, 3795, doi: [10.1093/mnras/stac285](https://doi.org/10.1093/mnras/stac285)
- Narayan, R., & McClintock, J. E. 2013, arXiv e-prints, arXiv:1312.6698. <https://arxiv.org/abs/1312.6698>
- Narayan, R., & Yi, I. 1994, *ApJL*, 428, L13, doi: [10.1086/187381](https://doi.org/10.1086/187381)
- Novikov, I. D., & Thorne, K. S. 1973, in *Black Holes (Les Astres Occlus)*, 343–450
- Pacucci, F., & Narayan, R. 2024, *ApJ*, 976, 96, doi: [10.3847/1538-4357/ad84f7](https://doi.org/10.3847/1538-4357/ad84f7)
- Pacucci, F., Nguyen, B., Carniani, S., Maiolino, R., & Fan, X. 2023, *ApJL*, 957, L3, doi: [10.3847/2041-8213/ad0158](https://doi.org/10.3847/2041-8213/ad0158)
- Peca, A., Vignali, C., Gilli, R., et al. 2021, *ApJ*, 906, 90, doi: [10.3847/1538-4357/abc9c7](https://doi.org/10.3847/1538-4357/abc9c7)
- Pesce, D. W., Palumbo, D. C. M., Narayan, R., et al. 2021, *ApJ*, 923, 260, doi: [10.3847/1538-4357/ac2eb5](https://doi.org/10.3847/1538-4357/ac2eb5)
- Power, C., Baugh, C. M., & Lacey, C. G. 2010, *MNRAS*, 406, 43, doi: [10.1111/j.1365-2966.2010.16481.x](https://doi.org/10.1111/j.1365-2966.2010.16481.x)

- Psaltis, D., Medeiros, L., Christian, P., et al. 2020, *PhRvL*, 125, 141104, doi: [10.1103/PhysRevLett.125.141104](https://doi.org/10.1103/PhysRevLett.125.141104)
- Reines, A. E., Condon, J. J., Darling, J., & Greene, J. E. 2020, *ApJ*, 888, 36, doi: [10.3847/1538-4357/ab4999](https://doi.org/10.3847/1538-4357/ab4999)
- Reines, A. E., Greene, J. E., & Geha, M. 2013, *ApJ*, 775, 116, doi: [10.1088/0004-637X/775/2/116](https://doi.org/10.1088/0004-637X/775/2/116)
- Reines, A. E., & Volonteri, M. 2015, *ApJ*, 813, doi: [10.1088/0004-637X/813/2/82](https://doi.org/10.1088/0004-637X/813/2/82)
- Ressler, S. M., Quataert, E., & Stone, J. M. 2018, *MNRAS*, 478, 3544, doi: [10.1093/mnras/sty1146](https://doi.org/10.1093/mnras/sty1146)
- Schawinski, K., Thomas, D., Sarzi, M., et al. 2007, *MNRAS*, 382, 1415, doi: [10.1111/j.1365-2966.2007.12487.x](https://doi.org/10.1111/j.1365-2966.2007.12487.x)
- Shakura, N. I., & Sunyaev, R. A. 1976, *MNRAS*, 175, 613
- Shang, Z., Brotherton, M. S., Wills, B. J., et al. 2011, *ApJS*, 196, 2, doi: [10.1088/0067-0049/196/1/2](https://doi.org/10.1088/0067-0049/196/1/2)
- Sijacki, D., Springel, V., Di Matteo, T., & Hernquist, L. 2007, *MNRAS*, 380, 877, doi: [10.1111/j.1365-2966.2007.12153.x](https://doi.org/10.1111/j.1365-2966.2007.12153.x)
- Thorne, K. S. 1974, *ApJ*, 191, 507, doi: [10.1086/152991](https://doi.org/10.1086/152991)
- Volonteri, M., & Rees, M. J. 2005, *ApJ*, 633, 624, doi: [10.1086/466521](https://doi.org/10.1086/466521)
- Yuan, F., Quataert, E., & Narayan, R. 2003, *ApJ*, 598, 301, doi: [10.1086/378716](https://doi.org/10.1086/378716)

APPENDIX

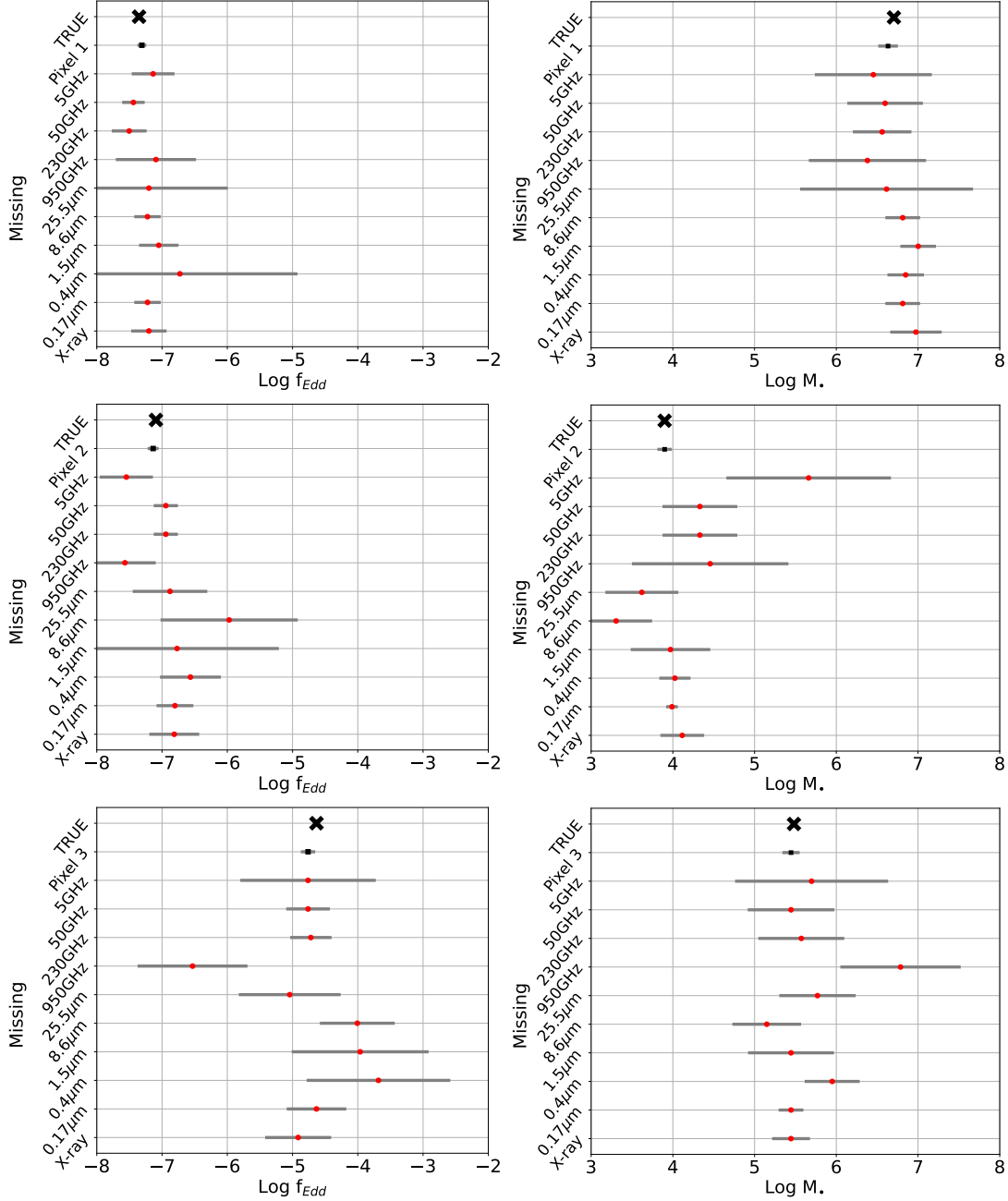
A. RANGES OF f_{Edd} AND M_{\bullet} IN CASE OF MISSING DATA

Figure 8. *Left panels:* Ranges of $\text{Log } f_{\text{Edd}}$ when a missing observation is recovered. The red circle represents the median of the distribution of possible $\text{Log } f_{\text{Edd}}$ values once the missing observation is recovered. The grey line covers the standard deviation of that distribution. The missing observations are listed on the y-axis. The label ‘TRUE’, indicated by a black cross, refers to the true value of the test BH residing in one of the five test pixels. The latter are listed on the second label on the y-axis. The median of the distribution of $\text{Log } f_{\text{Edd}}$ in that pixel is indicated by a black square, and the grey line represents the standard deviation of that distribution in that pixel. *Right panels:* Same as the left panels, but for $\log_{10} M_{\bullet}$ [M_{\odot}].

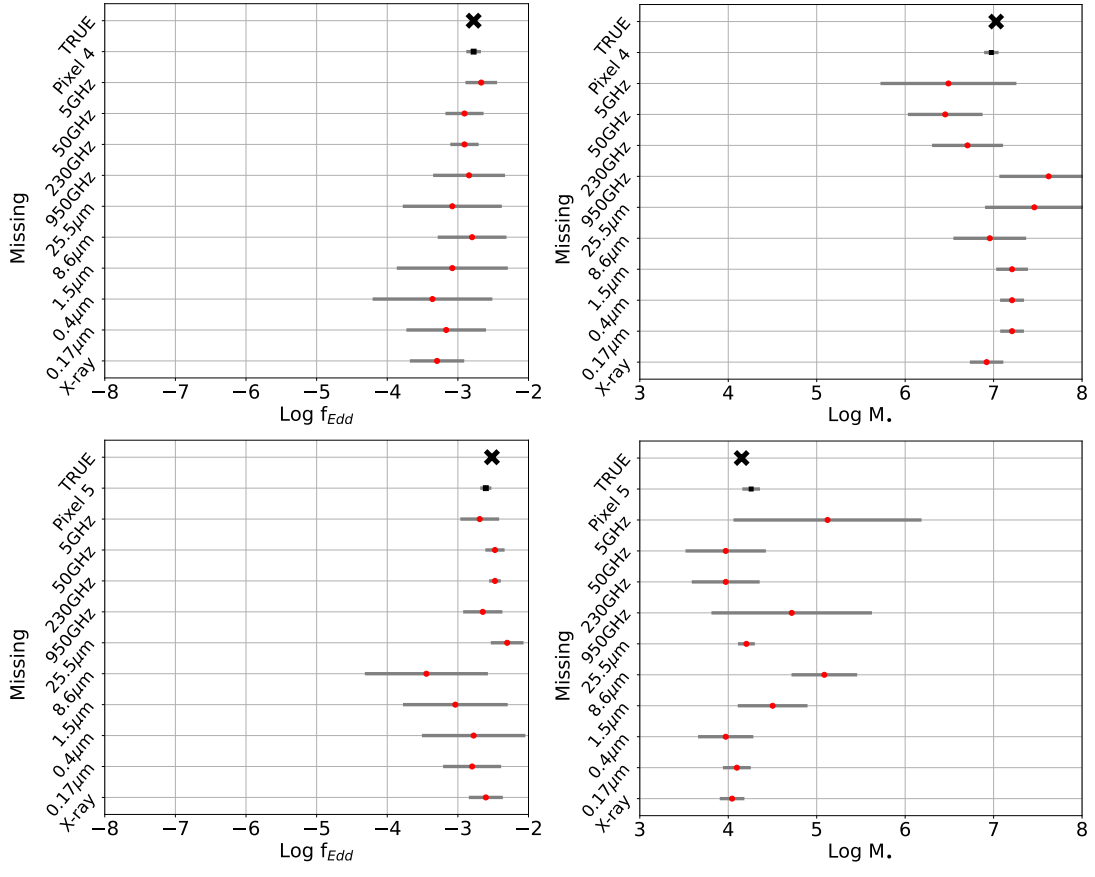


Figure 9. Same as Figure 8 but for test MBHs in pixels 4 and 5.

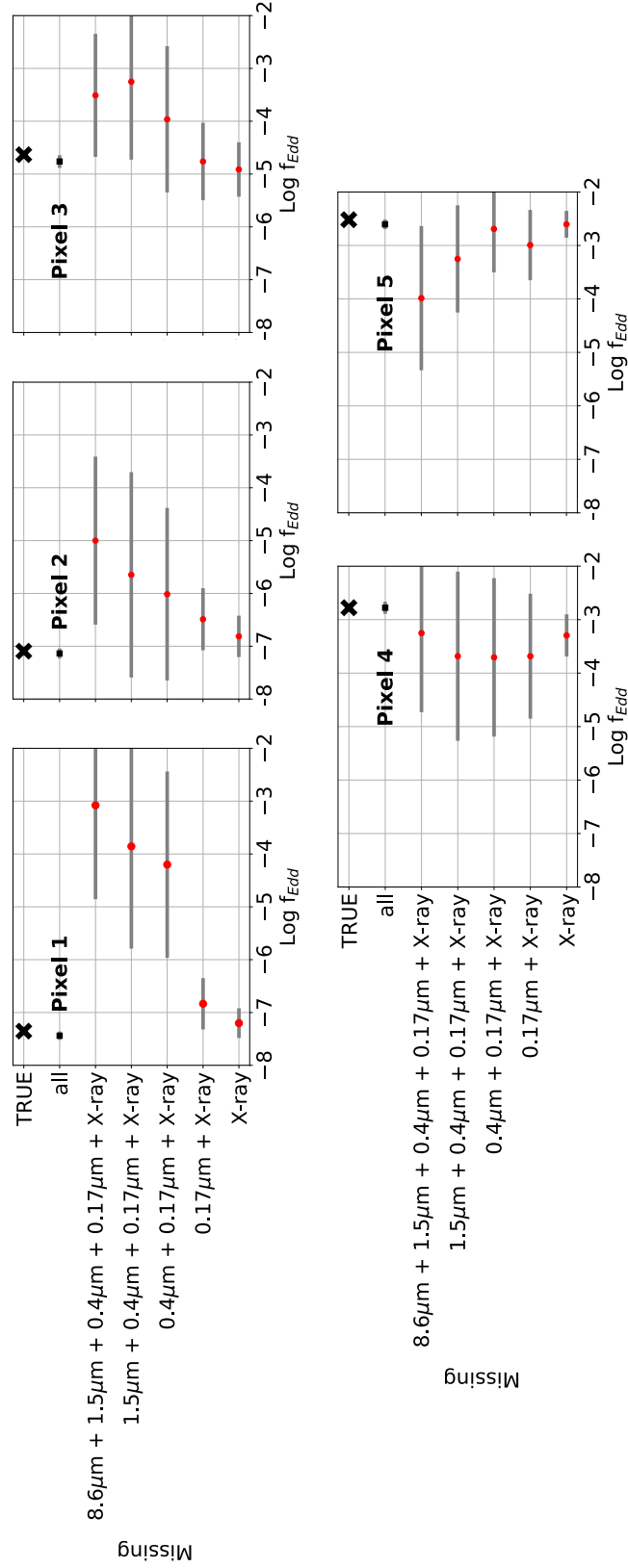


Figure 10. Range of $\text{Log } f_{\text{Edd}}$ for test MBHs from the five test pixels (indicated in bold text) in the case of recovered missing multiple observations, as listed on the y-axis. The black cross and square for the cases 'TRUE' and 'all' are the same as in Figures 8-9.

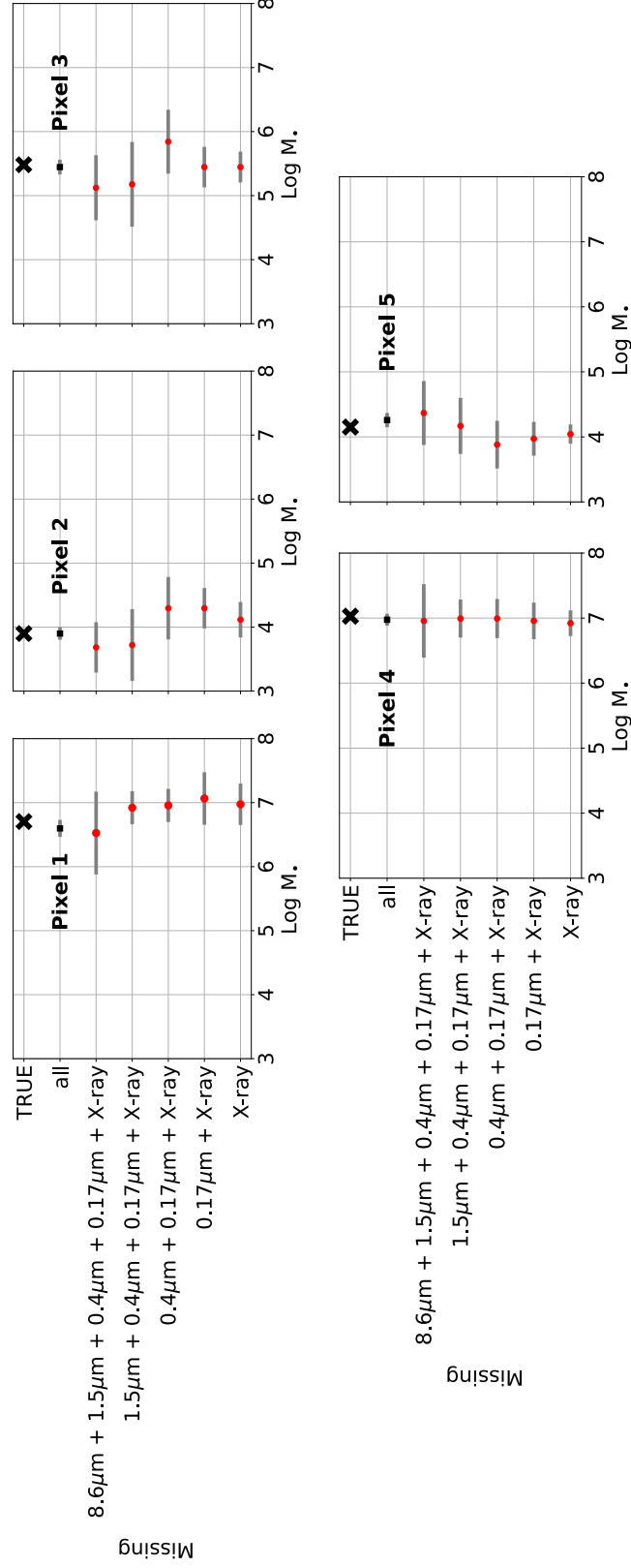


Figure 11. Same as in Figure 10 but for Log M_{\bullet} [M_{\odot}].